IEEE Access
Multidisciplinary | Rapid Review | Open Access Journal

Received August 4, 2019, accepted August 19, 2019, date of publication August 23, 2019, date of current version September 6, 2019.

Digital Object Identifier 10.1109/ACCESS.2019.2937095

A Programmable Optical Filter With Arbitrary Transmittance for Fast Spectroscopic Imaging and Spectral Data Post-Processing

JIAO LU[1], YUETIAN REN[1], WENBIN XU[2], XIAOYU CUI[1,3], LIPING XIE[1,3], SHUO CHEN[1,3], (Member, IEEE), JINHONG GUO[4], (Member, IEEE), AND YUDONG YAO[1,5], (Fellow, IEEE)

[1]College of Medicine and Biological Information Engineering, Northeastern University, Shenyang 110819, China
[2]Science and Technology on Optical Radiation Laboratory, Beijing 110854, China
[3]Key Laboratory of Data Analytics and Optimization for Smart Industry, Ministry of Education, Northeastern University, Shenyang 110819, China
[4]School of Information and Communication Engineering, University of Electronic Science and Technology of China, Chengdu 611731, China
[5]Department of Electrical and Computer Engineering, Stevens Institute of Technology, Hoboken, NJ 07030, USA

Corresponding author: Shuo Chen (chenshuo@bmie.neu.edu.cn)

This work was supported in part by the National Natural Science Foundation of China under Grant 61605025, Grant 61501101, and Grant 81501556, in part by the Innovative Research Groups of the National Natural Science Foundation of China under Grant 71621061, in part by the Science and Technology Foundation of National Defense Key Laboratory under Grant 61424080209, in part by the Program for Innovation Talents in Universities of Liaoning Province under Grant LR2016031, in part by the Ningbo Natural Science Foundation under Grant 2018A610365, in part by the Fundamental Research Funds for the Central Universities under Grant N171902001, Grant N171904006, and Grant N180719020, and in part by the 111 Project under Grant B16009.

ABSTRACT Spectral reconstruction method based on narrow-band measurements has been demonstrated to achieve ultrafast spectroscopic imaging with high spatial and spectral resolution, in which multiple narrow-band images are collected by using several specific filters. Although commercially available filters can be employed in such method, filters with complex transmittance that are difficult to be fabricated typically show significant improvement in spectral reconstruction accuracy. In this study, a two dimensional programmable optical filter based on digital micromirror device (DMD) is proposed, in which its transmittance spectrum can be arbitrarily and quickly switched to realize complex transmittance. Furthermore, its flexible transmittance enables directly hardware-based spectral data post-processing, which can perform data acquisition and analysis simultaneously. Those have been evaluated by the diffuse reflectance spectra from normal and occluded skin flaps, as well as Raman spectra from live, apoptosis and necrosis leukemia cells. Our simulation results show that much higher spectral reconstruction accuracies can be achieved by the optimized filters with complex transmittance. Furthermore, the classification accuracy by using the proposed method is comparable to those achieved by conventional numerical methods. Therefore, based on the proposed programmable optical filter, fast spectroscopic imaging with high spatial and spectral resolution can be achieved for observing fast changing phenomena and even real-time target identification.

INDEX TERMS Digital micromirror device, hyperspectral imaging, programmable optical filter, spectral reconstruction.

I. INTRODUCTION

Spectral imaging technique combines spectroscopy with conventional imaging, in which both spatial and spectral information can be collected simultaneously to form a three-dimensional spectral data cube [1]. By processing spectral data at each pixel, rich information about target sample can be extracted, thus the spectral imaging technique can be used in many areas, such as remote sensing [2], mineralogy [3], biomedicine [4], and astronomy [5]. According to different imaging modes, spectral imaging technology can be mainly cataloged into scanning based spectroscopic imaging [6] and snapshot spectroscopic imaging [7]. Scanning based spectroscopic imaging technologies only collect one-dimensional or two-dimensional subset of the complete three-dimensional spectral data cube for each scan, such as point-scanning [8], line-scanning [9] and staring [10], [11]. Therefore, it typically requires a large amount of scans to

The associate editor coordinating the review of this manuscript and approving it for publication was Valentina E. Balas.

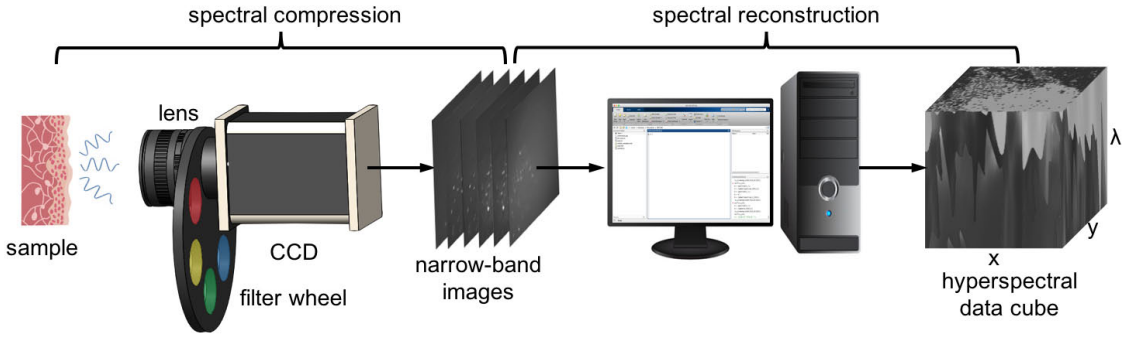

FIGURE 1. The schematic of the spectral reconstruction based spectroscopic imaging method.

obtain a complete spectral data cube, leading to slow data acquisition, especially when the required spatial and spectral resolution are high, which restricts its practical usage [12]. In contrast, snapshot spectroscopic imaging technologies typically capture both spatial and spectral information simultaneously in a snap shot [13], [7]. For example, the coded aperture snapshot spectral imaging(CASSI) [14], [15] utilizes a binary coded mask generated by DMD together with one or more dispersers to compress the three-dimensional hyperspectral data cube into a two-dimensional multiplexed projection, and the three-dimensional hyperspectral data cube can subsequently be demultiplexed numerically during post-processing. Thus, scanning is always avoided for such methods and the time efficiency of spectral image acquisition is significantly improved. However, most snapshot spectral imaging technologies require a large detector array to sample sufficient number of voxels and/or time-consuming post-processing procedure is necessary to recover the 3D spectral data cube [12].

Spectral reconstruction method based on narrow-band measurements is a potential solution for fast spectroscopic imaging with high spatial and spectral resolution [16]–[18]. This method compresses three-dimensional spectral image data into several narrow-band images through several specific filters in front of the CCD, and then reconstructs the spectrum at each pixel by using spectral reconstruction algorithms, as shown in Fig. 1. Since narrow-band measurements are used instead of the measurements at each wavelength, the signal-to-noise ratio can be significantly improved because of the intensity integration along the wavelength dimension [19]. Thus, lower requirements on the detector and high computational efficiency of the spectral reconstruction algorithms promote its ability to achieve fast spectroscopic imaging with high spatial and spectral resolution. In such method, the spectral compression efficiency of the filter sets and the spectral reconstruction efficiency of the spectral reconstruction algorithms are the two key factors that will affect the final accuracy of spectral measurements. According to our previous studies [16], [17], filter sets with optimal compression efficiency, such as non-negative principal components (PCs) based filters, are typically with complex transmittance, thus are not commercially available and even difficult to be produced by tunable filters. Although some studies have demonstrated that arbitrary transmittance can be achieved by a digital micromirror device (DMD) based setup, it only works for single point measurement [20], [21].

In this paper, a 2D programmable optical filter was designed and theoretically investigated to realize arbitrary transmittance by quickly switching the micromirrors on the digital micromirror device. The 2D programmable optical filter and its robustness were numerically assessed by using different configurations of incident light beam. The transmittance spectra of filter set for fast spectroscopic imaging was optimized by genetic algorithm and showed higher spectral reconstruction accuracy than commercially available filters, in which those complex transmittance spectra can only be achieved by programmable optical filters. Furthermore, programmable optical filter with specific transmittance was explored to perform hardware-based spectral data post-processing, in which narrow-band measurements were directly treated as the final coefficients for target identification instead of numerical post-processing followed by spectral data acquisition. By using such method, not only the spectral data acquisition and analysis can be further sped up, but also the difficulties in huge spectral data transmission and storage can be overcome. The programmable optical filter based spectral data post-processing was test on diffuse reflectance spectra from skin flaps and Raman spectra from leukemia cells. Excellent classification accuracies were achieved, which are comparable to those of conventional numerical methods.

Therefore, our contributions in this preliminary study can be summarized as: 1) a two-dimensional programmable optical filter with arbitrary transmittance is proposed, and its robustness with non-ideal incidence beams is theoretically investigated; 2) the spectral reconstruction accuracies for spectral reconstruction based spectroscopic imaging technique can be significantly improved by the complex transmittance of the proposed programmable optical filter; 3) hardware-based spectral data post-processing is theoretically investigated to substitute for the conventional numerical methods, thus the spectral data acquisition and

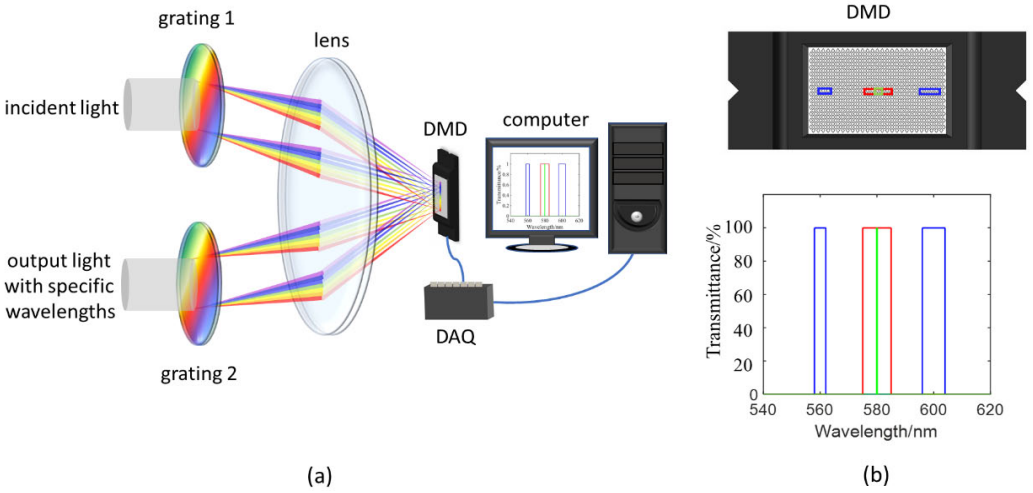

FIGURE 2. (a) Schematic of the DMD-based 2D programmable optical filter and (b) demonstration on achieving flexible binary filters by controlling micromirrors on the DMD.

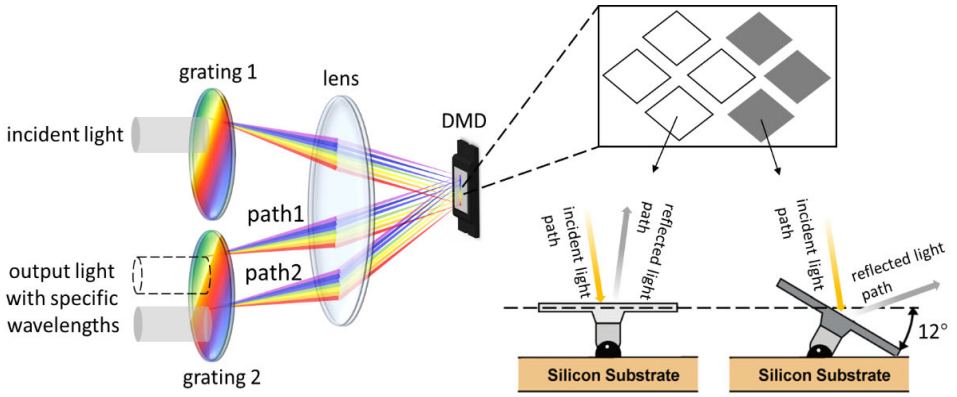

FIGURE 3. Optical path for wavelength selection when micromirror is inactive (path 1) or rotates +12° (path 2).

analysis can be performed simultaneously and sped up significantly.

II. MATERIALS AND METHODS

A. PROGRAMMABLE OPTICAL FILTER DESIGN

The schematic of the 2D programmable optical filter is shown in Fig. 2 (a), which consists of two gratings, a lens and a digital micromirror device (DMD). The gratings and DMD are placed at the focal plane on different sides of the lens, respectively. The collimated incident light beam first passes through diffraction grating 1 and disperses different wavelengths into different angles. Light with the same wavelengths from different positions on grating 1 are parallel and then are focused on the same micromirrors on DMD after passing through lens. After reflection by the selected micromirrors, light beam with specific wavelengths are emitted from grating 2 because of the reversibility of optical path. The DMD is used as a multi-spectral selector to select wavelengths of interest by setting the corresponding micromirrors to "on" orientation and to reject light with undesired wavelengths by setting the corresponding micromirrors to "off" orientation, as shown in Fig. 2 (b). Although DMD can only achieve binary transmittance at each time, arbitrary transmittance can theoretically be realized by modulating the micromirrors on the DMD while performing continuous exposure on CCD. The effective wavelength range and spectral resolution of the programmable optical filter are jointly determined by the groove density of grating, the focal length of lens, the effective area of DMD and the number of micromirrors within the effective area.

As shown in Fig. 3, the angles of light reflected from DMD should alter 24°, due to +12° rotation of micromirrors during the wavelength selection. However, after the reflected light passing through lens, the angles of light at each wavelength when micromirrors rotate +12° (path 2 in Fig. 3) become exactly the same to those when micromirrors are inactive with 0° flat (path 1 in Fig. 3). The reason is that the light from the same position on the focal plane should form a collimated beam after passing through the lens and the direction of such collimated beam is only determined by the position on the

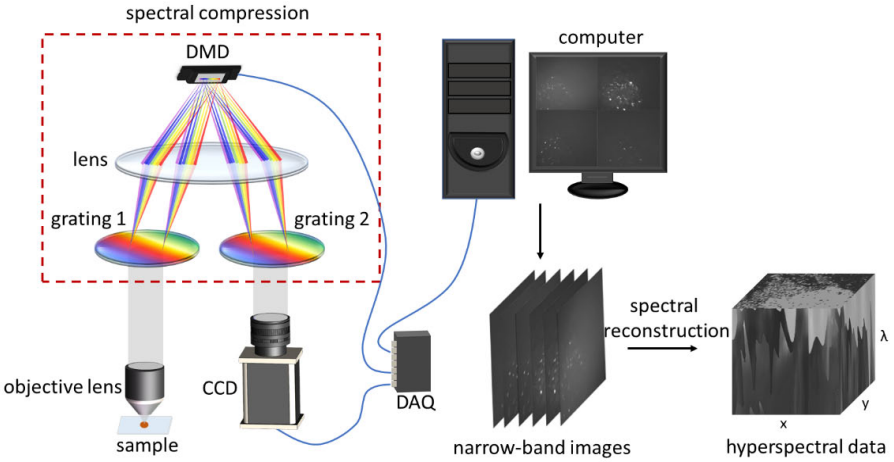

FIGURE 4. Schematic of spectral reconstruction method based on narrow-band measurements.

focal plane that the light comes from. Although light with selected wavelengths is indeed directed to different positions on grating 2 due to $+12°$ rotation of micromirrors, only the position of beam is shifted and the beam size is shrunk or enlarged. Since those changes are non-essential for evaluating the proposed programable optical filter, the micromirror was simplified to 'on' and 'off' state without rotation in the numerical simulation, in which 'on' state micromirror reflects light while 'off' state micromirror does not.

In this study, two sets of configurations for each optical component were used to numerically simulate two sets of filters with spectral range of 470nm to 700nm for diffuse reflectance measurements and spectral range of 830nm to 910nm for Raman measurements, respectively. In both simulations, DMD with 912×1140 micromirrors (DLP4500, Texas Instruments) was used, in which the size of each micromirror is $7.6\mu m\times7.6\mu m$ and the diagonal length is $10.8\mu m$. Each micromirror can be controlled to rotate $\pm12°$ from inactive position at a binary pattern rate of 4.2KHz. Thus, such high modulation rate can promote fast switching of the transmittance of the proposed programmable optical filter. In this study, the smallest step size of the transmittance was set to 0.1%, hence at least four different filters can be theoretically carried out in 1 second. In order to match the spectral range to the size of effective area on DMD, the focal length of the lens and the groove density of gratings were optimized. For diffuse reflectance measurements, the focal length was optimized to 35mm and the groove density was set to 800 lines/mm. For Raman measurements, the focal length was optimized to 50mm and the groove density was set to 800 lines/mm.

In the current setup as described above, the proposed programmable optical filter is designed particularly for the collimated light with perpendicular incidence, which may not be the case in all practical applications, e.g. microscope setups. In order to verify the robustness of the proposed programmable optical filter, two different forms of incident light, i.e. collimated beam with non-perpendicular incidence and uncollimated beam, were used to obtain the band-pass transmittance, respectively. Their central wavelengths and bandwidths were analyzed and compared to those reference results by using collimated light with perpendicular incidence.

B. PROGRAMMABLE OPTICAL FILTER BASED FAST SPECTROSCOPIC IMAGING

For fast spectroscopic imaging, spectral reconstruction method based on narrow-band measurements were used [16]–[18], and the schematic of this method is shown in Fig. 4. This method first employs several specific filters to compresses three-dimensional spectral image data cube into several narrow-band images and then reconstructs the spectrum at each pixel by using spectral reconstruction algorithms. The narrow-band measurements are collected by the CCD after the light passing through specific filters. Those specific filters can be replaced by the proposed programmable optical filter, which is expected to achieve a better spectral compression efficiency and consequent better spectral reconstruction accuracy. Since the filter can be fully characterized by its transmission, the narrow-band measurements N can be numerically synthesized as the inner product of the spectra S and the filters' transmittance F, as in Eq. (1).

$$N = SF \tag{1}$$

Since such spectral reconstruction method is a supervised learning method in nature, calibration data set is always necessary to build the mathematical model to link the narrow-band measurements and the corresponding spectra in the calibration stage. Wiener estimation is one of the most frequently used spectral reconstruction methods because of its time efficiency. Wiener matrix, i.e. the mathematical model to link the narrow-band measurements and the spectra, was extracted from the narrow-band measurements N and spectrum S in the calibration data set according to Eq. (2), in which $E()$ represents the ensemble average. The Wiener

matrix was subsequently applied on the narrow-band measurements in the test data set to obtain the reconstructed spectrum at each pixel, in which the final reconstructed spectrum is calculated by the multiplication between narrow-band measurements and Wiener matrix.

$$W = E(SN^T)[E(NN^T)]^{-1} \tag{2}$$

In this study, the spectral reconstruction accuracies by using commercially available filters, non-negative PCs based filters and filters optimized by genetic algorithm were analyzed and compared. For the commercially available filters, the transmittance spectra of 3CCD (AT-200 GE, JAI, Japan) were used for diffuse reflectance measurements [22], whereas the transmittance spectra of 6 filters optimized from 37 commercially available filters from five companies were used for Raman measurements. More specifically, those 37 filters included two filters (D850/20m, D850/40m) from Chroma Technique Cooperation (Bellows Falls, VT, US), two filters (NT84-790, NT84-791) from Edmund Optics (Barrington, NJ, US), eleven filters (3RD850LP, 3RD900LP, XB142, XB143, XB146, XB149, XF3308, XL19, XL40, XLK18, XLK20) from Omega Filters (Brattleboro, VT, US), six filters (FF01-830/2-25, FF01-832/37-25, FF01-835/70-25, FF01-840/12-25, FF 01-857/30-25, FF01-910/5-25) from Semrock (Rochester, NY, US), sixteen filters (FB830-10, FB840-10, FB850-10, FB850-40, FB860-10, FB870-10, FB880-10, FB880-40, FB890-10, FB900-40, FB 910-10, FL830-10, FL850-10, FL880-10, FL 905-10, FL905-25) from Thorlabs (Newton, New Jersey, US). More details about those 37 commercially available filters can be found in reference [16]. The transmittance spectra of non-negative PCs based filters were derived from the principal component analysis (PCA) of spectra measured from representative target samples, thus the resulting narrow-band measurements can benefit from the optimal compression properties of the PCA scheme [23], [24]. In order to achieve a better spectral compression efficiency and spectral reconstruction accuracy, the filters were further optimized by genetic algorithm. The initial population of filters were generated based on the non-negative PCs based filters and their variants, and then evolve with crossover rate of 90% and mutation rate of 10%. Leave-one-out method was used for cross validation in an unbiased manner, and the mean relative root mean square error (RMSE) [25] between the reconstructed spectra and the reference spectra was treated as the criterion to judge the spectral reconstruction accuracy. More specifically for Raman measurements, the fluorescence background was removed by using a fifth-order polynomial fitting [26] for both reconstructed Raman spectra and reference Raman spectra before the calculation of mean relative RMSE. Besides collimated light with perpendicular incidence configuration, distorted transmittance spectra generated by collimated beams with non-perpendicular incidence and uncollimated beam were employed as well to investigate their impact on spectral reconstruction accuracy.

C. PROGRAMMABLE OPTICAL FILTER BASED SPECTRAL DATA POST-PROCESSING

The schematic of the programmable optical filter based spectral data post-processing is shown in Fig. 5. By coding the spectral information with specific transmittance of programmable optical filter, named as coding transmittance, only the critical spectral information about decision making in the classification can be specifically collected, which is similar to the identification of target object with certain color through glasses with exact the same color. This approach integrates the spectral data post-processing into spectral data collection, in which the spectral data acquisition and analysis can be sped up significantly. Since only a few narrow-band images is needed to be collected instead of the huge spectral data cube, the requirements on spectral data transmission and storage can be much lower. The transmittance of the programmable optical filter was derived based on the combination of PCA and linear discriminant analysis (LDA) methods. In this way, the narrow-band measurements by using such transmittance can be equivalent to the linear discriminate scores of the conventional PCA-LDA method, in which those linear discriminate scores [27] are typically used for decision making in the classification. Thus, those narrow-band measurements are expected to collect critical spectral information and can be directly used for decision making in the classification. The detailed procedure of the coding transmittance generation is as follows:

Step 1: The principal eigenvector U_1 and principal eigenvalue s were derived based on PCA method. Firstly, the covariance D of the target hyperspectral data H is calculated according to Eq. (3).

$$D = \overline{H}\,\overline{H}^T \tag{3}$$

where $\overline{H}$ is the normalized matrix of the target hyperspectral data H, and the superscript 'T' represents matrix transpose. Thereafter, eigenvectors of the covariance matrix D are arranged from large to small according to corresponding eigenvalues, and the principal eigenvector U_1 consisted of the first k-th constituent eigenvectors. The principal eigenvalues s, i.e. the result after hyperspectral data dimension reduction, can be calculated according to Eq. (4).

$$s = HU_1 \tag{4}$$

Step 2: The transformation vector U_2 is obtained based on LDA algorithm. Firstly, the within-class scatter matrix M_σ is calculated according to Eq. (5).

$$M_\sigma = \sum\sum (s_{ij} - u_i)(s_{ij} - u_i)^T \tag{5}$$

where s_{ij} refers to the j-th element of the i-th category's principal eigenvalues, and u_i refers to the average of the i-th category's principal eigenvalues. Then, the between-class scatter matrix M_τ is calculated according to Eq. (6).

$$M_\tau = \sum (u_i - u)(u_i - u)^T \tag{6}$$

where u is average of all categories' principal eigenvalues. Finally, find the largest eigenvalue in the matrix of $M_\sigma M_\tau$,

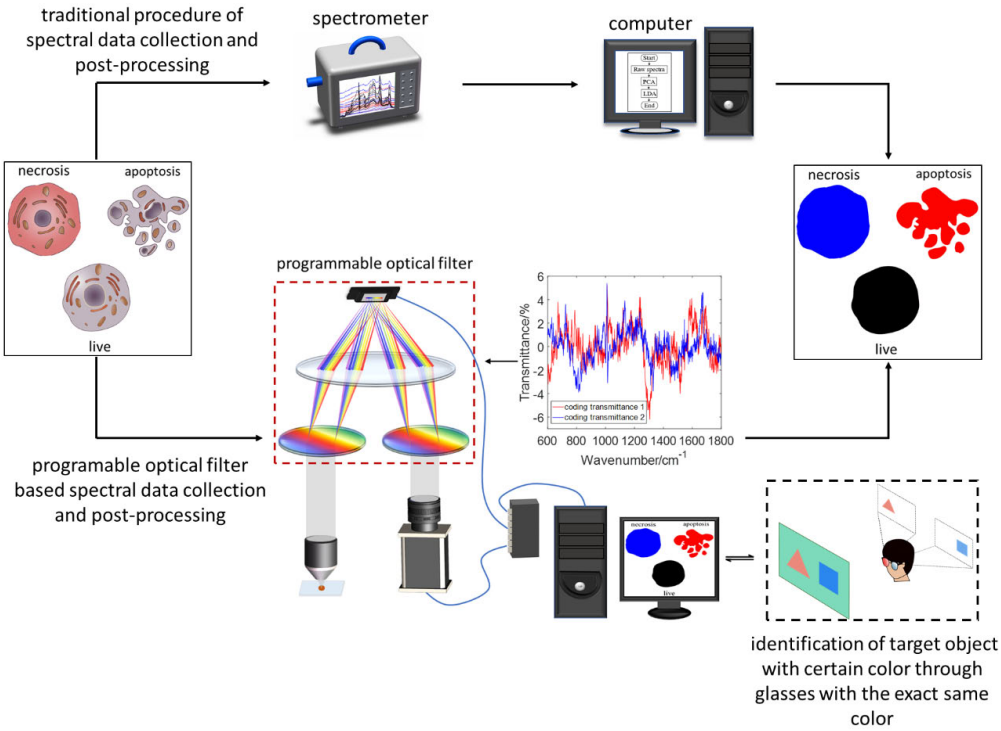

FIGURE 5. Comparison between the traditional procedure of spectral data collection and post-processing and programable optical filter based spectral data collection and post-processing: The function of coding transmittance is to employed to specifically collect the critical spectral information about classification decision making, which is similar to the identification of target object with certain color through glasses with the exact same color.

in which the eigenvector corresponding to this largest eigenvalue is treated as the transformation vector U_2.

Step 3: The coding transmittance T is generated based on the principal eigenvector U_1 and transformation vector U_2. It should be noted that the number of coding transmittance spectra in T should be the identical to the number of categories to be differentiated subtracted by 1.

$$T = U_1 U_2 \tag{7}$$

Since the proposed programmable optical filter can only achieve non-negative transmittance, the compensation transmittance T_1 is typically necessary to generate a non-negative imaging transmittance T_2 by raising all transmittance at each wavelength.

$$T_2 = T + T_1 \tag{8}$$

where T_1 is the absolute value of the minimum value in T. Thus, the final narrow-band images for classification are the subtraction between imaging narrow-band images and compensation narrow-band images, in which the imaging narrow-band images and compensation narrow-band images are the narrow-band images collected via imaging transmittance and compensation transmittance respectively.

The synthesized narrow-band measurements based on the above coding transmittance are directly used to evaluate the hardware-based spectral data post-processing capability by the final classification accuracy. Besides collimated light with perpendicular incidence configuration, distorted transmittance spectra generated by collimated beams with non-perpendicular incidence and uncollimated beam were employed as well to theoretically investigate their impact on final classification accuracy.

D. SAMPLE PREPARATIONS AND SPECTRAL MEASUREMENTS

To demonstrate the spectral compression efficiency in spectral reconstruction based spectroscopic imaging and the spectral data post-processing capability of the proposed programmable optical filter, diffuse reflectance spectra from skin flaps and Raman spectra from leukemia cells were used for numerical simulation. The diffuse reflectance spectra were measured from normal and occluded skin flaps with a wavelength range of 470nm to 700nm, as shown in Fig. 6 (a). The number of spectral measurements from occluded group was 83 and the number of spectral measurements from control group was 19, in which the spectral measurements were taken at 15 minutes after flap surgery. The details of experiment preparation and spectral measurements can be found in reference [28]. Raman spectra were measured from human chronic myelogenous leukemia cells (K562 cell line) with a range of 600 cm^{-1} to 1800 cm^{-1}, as shown in Fig. 6 (b). The excitation wavelength was 785nm and the exposure time was 10s accumulated 6 times. The cells were treated with different drugs to induce apoptosis and necrosis. Ten Raman

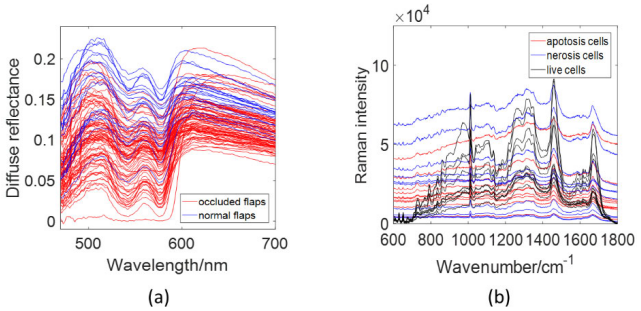

FIGURE 6. Two sets of spectra are used to demonstrate the programmable optical filter based spectral data post-processing: (a) diffuse reflectance spectra from normal and occluded skin flaps and (b) Raman spectra from live, apoptosis and necrosis leukemia cells.

spectra were collected from apoptosis, necrosis and live cells respectively, thus a total number of 30 Raman measurements were acquired. The details of experiment preparation and spectral measurements have been described elsewhere [29]. In this study, the narrow-band measurements were numerically synthesized as the inner product of the measured spectra and the transmittance spectra of the programable optical filter.

All the above simulations were implemented in MATLAB (R2016a, MathWork) on a computer with Intel Core i5-7200U 2.5GHz CPU, 8GB RAM, and Windows 10 operating system.

III. RESULTS AND DISCUSSIONS

A. THE PERFORMANCE AND ROBUSTNESS OF PROGRAMMABLE OPTICAL FILTER

In order to evaluate the performance and robustness of programmable optical filter, the focal length of lens and groove density of gratings were optimized with a collimated light with perpendicular incident, to match the spectral range to the size of effective area on DMD. For diffuse reflectance measurements, the focal length was optimized to 35mm and the groove density was set to 800 lines/mm, in which dispersed wavelengths from 470nm to 700nm were occupied to 876 micromirrors on the DMD and the theoretical spectral resolution is 0.4nm. For Raman measurements, the focal length was optimized to 50mm and the groove density was set to 800 lines/mm, in which dispersed wavelengths from 830nm to 910nm were assigned to 805 micromirrors on the DMD and the theoretical resolution is 0.2nm. Those optimized results of collimated light with perpendicular incident were served as reference and compared with the result of three different forms of incident light, i.e. collimated beams with non-perpendicular incidence, convergent beam and divergent beam.

1) COLLIMATED BEAM WITH NON-PERPENDICULAR INCIDENCE

Table 1 shows the comparison between the central wavelengths of collimated beam with non-perpendicular incidence and the reference central wavelengths for diffuse reflectance configuration. For different reference central wavelengths, there are different central wavelength shifts when inducing different incident angles, i.e. the wavelength shifts are approximately 10nm, 20nm and 40nm for incident angles of ±0.5°, ±1° and ±2°, respectively. Thus, with the increasement of incident angle, the central wavelengths shift further away from the reference central wavelengths. The wavelengths become larger when the incident angles are positive, whereas the wavelengths become smaller when the incident angles are negative, in which the positive and negative incident angle refer to different sides of the optical axis. Moreover, due to the limited effective area of DMD, an excessively large incident angle will cause significant mismatch between the spectral range and the size of effective area on DMD, and the actual central wavelength is beyond the expected spectral range. However, only slight changes on bandwidth are observed as shown in Table 2. According to Table 2, the variations of bandwidths are similar for different reference bandwidths as well as for different central wavelengths, when the incident angle is fixed.

Similar findings can also be observed with Raman configurations, as shown in Tables 3 and 4. Although smaller spectral range is used for the Raman configurations, the shifts of central wavelength are similar to that of diffuse reflectance configuration, i.e. the wavelength shifts are approximately 10nm, 20nm and 40nm for incident angles of ±0.5°, ±1° and ±2° respectively. However, in contrast to diffuse reflectance configurations, there's almost no bandwidth change for Raman configurations when the incident angle of the collimated

TABLE 1. Comparison between the central wavelengths of collimated beam with non-perpendicular incidence and reference central wavelengths for diffuse reflectance configuration.

Incident angle (°)	Central wavelengths (nm)			
Reference (0°)	**500**	**550**	**600**	**650**
0.5	511	560.8	611	660.8
1	521.9	571.7	621.9	671.8
2	543.7	593.5	643.7	693.6
-0.5	489.1	539	589.2	639
-1	478.2	528.1	578.3	628.1
-2	-	506.3	556.5	606.3

TABLE 2. Comparison between the bandwidths of collimated beam with 1° incident angle and reference bandwidths for diffuse reflectance configuration.

Reference bandwidths (nm)	Bandwidths of collimated beam with 1° incident angle with different central wavelengths (nm)			
	500	550	600	650
1	1.3	1.1	1.2	1.1
5	5.2	5.2	5.1	5.2
10	10.3	9.9	10	10

TABLE 3. Comparison between the central wavelengths of collimated beam with non-perpendicular incidence and the reference central wavelengths for Raman configuration.

Incident angle (°)	Central wavelengths (nm)						
Reference (0°)	**840**	**850**	**860**	**870**	**880**	**890**	**900**
2	883.6	893.6	903.6	-	-	-	-
1	861.8	871.8	881.8	891.8	901.9	-	-
0.5	850.9	860.9	870.9	880.9	891	900.9	-
-0.5	-	839.1	849.1	859.1	869.1	879.1	889.1
1	-	-	838.1	848.2	858.2	868.2	878.2
2	-	-	-	-	836.4	846.4	856.4

TABLE 4. Comparison between the bandwidths of collimated beam with 1° incident angle and the reference bandwidths for Raman configuration.

Reference bandwidths (nm)	Bandwidths of collimated beam with 1° incident angle with different central wavelengths (nm)				
	840	850	860	870	880
1	1	1.1	0.9	1	1
5	5	5	5	5	5
10	10	10	10	10	10

beam is 1°. Compared the results of diffuse reflectance configuration in Tables 1 and 2 with the results of Raman configuration in Tables 3 and 4, it can be observed that the fluctuations are slightly larger for diffuse reflectance configuration among each row in Tables 1 and 2. This is attributed to the fact that the micromirrors are assumed to be discretely distributed on the DMD in the numerical simulation. Since the size and the number of micromirrors have already been fixed for both the simulations of diffuse reflectance configuration and Raman configuration, the wider wavelength range for diffuse reflectance configuration will definitely lead to a larger step size of wavelength during the simulation, and will further cause slightly larger fluctuations among the results of diffuse reflectance configuration in Tables 1 and 2.

2) UNCOLLIMATED BEAM

Both convergent and divergent beams can be treated as the uncollimated beam in the numerical simulation. The reason is that maximum incident angles on both sides of optical axis are exactly the same when the divergence and convergence angles are the same. Thus, the convergent beam consists of boundary A and B should be equivalent to divergent beam consisted of boundary B and C after translating the convergent beam boundary A with a certain distance along the grating, as shown in Fig. 7. Since only the central wavelength and bandwidth are considered for evaluating the performance of the proposed programmable optical filter, the final simulated results for both convergent and divergent beams should be identical if divergence and convergence angles

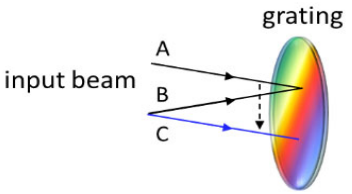

FIGURE 7. Illustration of the convergent beam and divergent beam entering the grating.

TABLE 5. Comparison between the central wavelengths of uncollimated beam and the reference central wavelengths for diffuse reflectance configuration.

Convergence or Divergence angle (°)	Central wavelengths (nm)			
Reference (0°)	**500**	**550**	**600**	**650**
0.5	500.05	549.9	600.1	649.95
1°	500	549.9	600.1	649.9
2°	500.05	549.9	600.1	649.9

TABLE 6. Comparison between the bandwidths of uncollimated beam with 1° convergence/divergence angle and the reference bandwidths for diffuse reflectance configuration.

Reference Bandwidths (nm)	Bandwidths of uncollimated beam with 1° convergence/divergence angle with different central wavelengths (nm)			
	500	550	600	650
1	23.2	22.9	23	23
5	27	27	26.9	27
10	32.1	31.8	31.9	31.8

are the same. This has also been verified by our numerical simulation.

Table 5 shows the comparison between the central wavelengths of uncollimated light and the reference central wavelengths for diffuse reflectance configuration. It can be observed that central wavelengths remain unchanged with different convergence/divergence angles.

TABLE 7. Comparison between the central wavelengths of uncollimated beam and the reference central wavelengths for Raman configuration.

Convergence or Divergence angle (°)	Central wavelengths (nm)						
Reference (0°)	**840**	**850**	**860**	**870**	**880**	**890**	**900**
0.5°	839.95	850	859.95	870.05	880.05	890.05	900.05
1°	841.05	850	860	870	880.05	890	898.95
2°	846.5	851.1	859.95	870	880.05	888.95	893.5

TABLE 8. Comparison between the bandwidths of uncollimated beam with 1° convergence/divergence angle and the reference bandwidths for Raman configuration.

Reference Bandwidths (nm)	Bandwidths of uncollimated beam with 1° convergence/divergence angle with different central wavelengths (nm)						
	840	850	860	870	880	980	900
1	20.6	22.8	22.8	22.8	22.8	22.8	20.6
5	23.4	26.9	26.8	26.8	26.8	26.8	23.4
10	25.9	31.8	31.8	31.8	31.8	31.8	25.9

However, compared with reference bandwidths, the bandwidth become much larger when inducing uncollimated beam, as shown in Table 6. The reason is that the uncollimated light, which can be treated as the light with continuously different incident angles, will lead to an illumination with a broader spectral range on each micromirrors on the DMD. In addition, with the increasement of convergence/divergence angle, the bandwidths become broader, whereas only slight bandwidth changes can be found among different central wavelengths. When inducing uncollimated beam with 1° convergence/divergence angle, the bandwidths for diffuse reflectance configurations are approximately 23nm, 27nm and 32nm instead of reference bandwidths of 1nm, 5nm and 10nm, respectively.

Similar findings can also be observed with Raman configurations, as shown in Tables 7 and 8. Although the spectral range for the Raman configurations is only around 1/3 of that for diffuse reflectance configuration, the bandwidths for Raman configuration are only slightly smaller than that for diffuse reflectance configuration, i.e. the bandwidths are approximately 22.8nm, 26.8nm and 31.8nm in most cases for reference bandwidths of 1nm, 5nm and 10nm respectively. However, there is sharp decrease of bandwidths with the central wavelengths of 840nm and 900nm compared to other central wavelengths, and decrement is larger as the divergence/convergence angle increases. This is because that only wavelengths within spectral range of 830nm to 910nm are considered in the numerical simulation, thus some resulting wavelengths are beyond the spectral range when the central wavelength is close to the boundary of spectral range.

Based on the above numerical simulations and analysis, it can be concluded that the changes of incident angle are more likely to cause severe changes on central wavelengths, whereas uncollimated beam are more likely to induce severe changes on bandwidths. Thus, both incident angle and beam collimation need to be calibrated beforehand. The calibration can be easily performed by measuring the spectrum with a spectrometer after a broadband light beam passing through the programmable optical filter when certain micromirror is with 'on' state, and then the programmable optical filter can be quantitively calibrated based on the above simulated reference results.

B. SPECTRAL RECONSTRUCTION BASED ON PROGRAMMABLE OPTICAL FILTER

Table 9 shows the comparison of the spectral reconstruction accuracies for diffuse reflectance and Raman measurements by using different types of filters. It is assumed that the non-negative PCs based filters and filters optimized by genetic algorithm are fabricated by the proposed programmable optical filter due to their complex transmittance, thus configurations of collimated beam with non-perpendicular incidence and uncollimated beam are employed as well to investigate their impact on spectral reconstruction accuracy. For diffuse reflectance measurements, the mean relative RMSEs are 2.0801×10^{-2}, 2.0601×10^{-2} and 2.0589×10^{-2} when using commercial filters, non-negative PCs based filters and filters optimized by genetic algorithm, respectively. There's only slight improvement when using filters optimized by genetic algorithm,

TABLE 9. Comparison of the spectral reconstruction accuracies for diffuse reflectance and Raman measurements by using different types of filters.

	Commercial filters	Non-negative PCs based filters	Filters optimized by genetic algorithm
Mean Relative RMSE for diffuse reflectance measurements (Reference)	2.0801×10^{-2}	2.0601×10^{-2}	2.0589×10^{-2}
Mean Relative RMSE for diffuse reflectance measurements (0.5° Incidence)	-	2.1500×10^{-2}	2.1441×10^{-2}
Mean Relative RMSE for diffuse reflectance measurements (0.5° Convergence)	-	2.0608×10^{-2}	2.0593×10^{-2}
Mean Relative RMSE for Raman measurements (Reference)	3.4912×10^{-2}	2.9335×10^{-2}	2.8075×10^{-2}
Mean Relative RMSE for Raman measurements (0.5° Incidence)	-	7.3215×10^{-2}	6.4372×10^{-2}
Mean Relative RMSE for Raman measurements (0.5° Convergence)	-	3.4821×10^{-2}	3.2175×10^{-2}

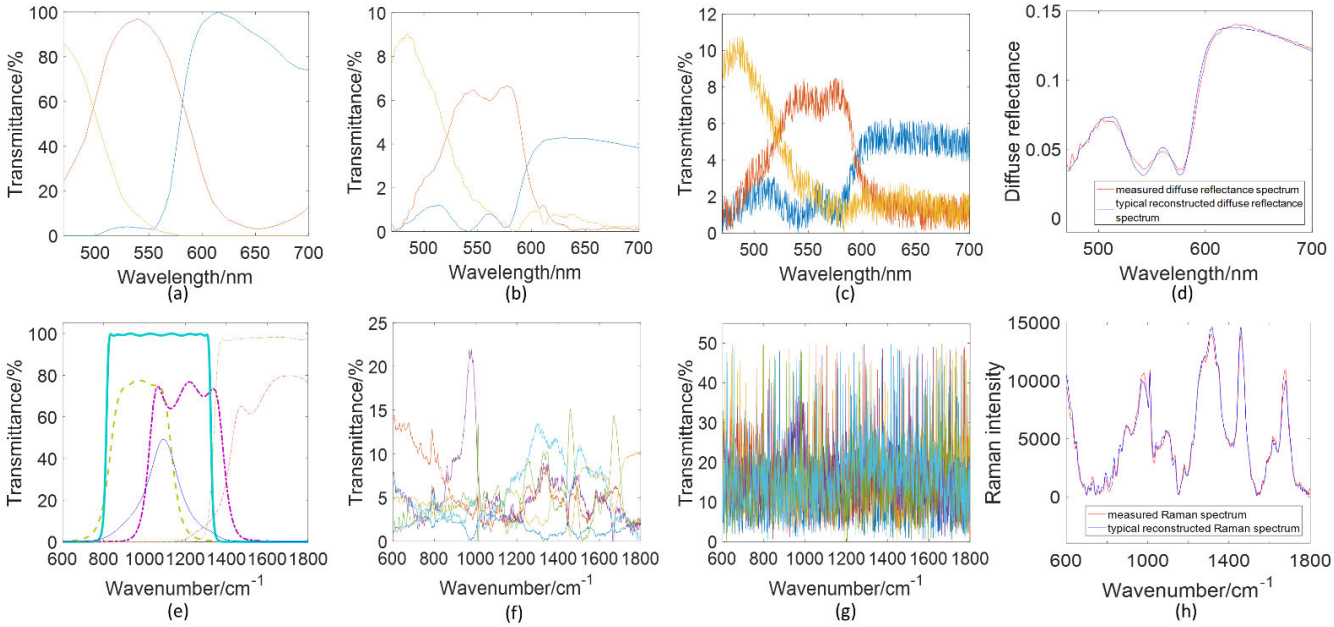

FIGURE 8. Transmittance spectra of (a) commercial filters, (b) non-negative PCs based filters, (c) filters optimized by genetic algorithm for diffuse reflectance measurements and (d) typical reconstructed diffuse reflectance spectrum by using filters optimized by genetic algorithm; Transmittance spectra of (e) commercial filters, (f) non-negative PCs based filters, (g) filters optimized by genetic algorithm for Raman measurements and (h) typical reconstructed Raman spectrum by using filters optimized by genetic algorithm.

whereas the transmittance spectra of these optimized filters are much more complex compared with commercial filters and non-negative PCs based filters, as shown in Fig. 8 (a) to (c). The reason is that the spectral shape of diffuse reflectance spectra for the skin flap is uncomplicated and it only carries a small amount of spectral information, thus simple transmittance is sufficient to compress the important spectral information, which is also verified by the transmittance spectra of the corresponding non-negative PCs based filters. In Fig. 8 (d), it has demonstrated the excellent agreement between the measured diffuse reflectance spectrum and the typical diffuse reflectance spectrum reconstructed by using filters optimized by genetic algorithm, in which the relative RMSE for the typical reconstructed diffuse reflectance spectrum is 2.0381×10^{-2} and is closest to the mean relative RMSE. For Raman measurements, the mean relative RMSEs are 3.4912×10^{-2}, 2.9335×10^{-2} and 2.8502×10^{-2} when using commercial filters, non-negative PCs based filters and filters optimized by genetic algorithm, respectively. Although the transmittance spectra of the filters optimized by genetic algorithm and non-negative PCs based filters are much more complex as shown in Fig. 8 (f) and (g), they show significant improvement of 19.6% and 16.0% compared to commercial filters, respectively. The reason is that the spectral shape of Raman spectra for the leukemia cells is very complicated due to those sharp Raman peaks and

a large amount of spectral information within those complex Raman spectra, thus complicated transmittance is indeed necessary to fully compress the important spectral information, which can also be verified by the transmittance spectra of non-negative PCs based filters. In Fig. 8 (h), it has demonstrated the excellent agreement between the measured Raman spectrum and the typical Raman spectrum reconstructed by the filters optimized by genetic algorithm, in which the relative RMSE for the typical reconstructed Raman spectrum is 2.7841×10^{-2} and is closest to the mean relative RMSE. For both diffuse reflectance and Raman measurements, the distorted transmittance by uncollimated beam always show much less degradation on spectral reconstruction accuracies than distorted transmittance by collimated light with non-perpendicular incidence. This could be attributed to the fact that the distorted transmittance by uncollimated beam can still collect most of the important spectral information although the larger bandwidth leads to the collection of some useless spectral information, whereas the distorted transmittance by collimated beam with non-perpendicular incidence loses the most important spectral information due to the central wavelength shifts. In addition, it should be noted that those filters optimized by genetic algorithm might not perform the overall optimized spectral reconstruction because genetic algorithm can only find the locally optimal solution. Furthermore, the initial population are generated based on the non-negative PCs based filters and their variants, and the compression efficiency is already optimal by such PCA scheme, thus there's only slight improvement by using the genetic algorithm. It is expected that much higher spectral reconstruction accuracy can be achieved if a fully random initial population are used, however much larger population size is indeed necessary since the extremely large amount of possibilities of different transmittance. According to the above results, the complexity of transmittance is increased with the complexity of the spectral shape and the amount of spectral information within the spectra, thus the proposed programmable optical filter would be very useful for the fast spectroscopic imaging with complicated spectral shape, such as Raman imaging.

At present, scanning based techniques, such as point-scanning, line-scanning and staring, are the most frequently used method in the commercial hyperspectral imaging systems, which only collect one-dimensional or two-dimensional subset of the complete three-dimensional hyperspectral data cube during each scan. A large amount of scans are required to collect the spectral and spatial information for the entire region of interest and the entire spectral range, thus the acquisition of hyperspectral images is very time-consuming, especially when a high spatial and spectral resolution is required. Although snapshot spectroscopic imaging technologies typically capture both spatial and spectral information simultaneously in a snap shot, most snapshot spectral imaging technologies require a large detectors array to sample sufficient number of voxels and/or time-consuming post-processing. Our spectral reconstruction based method only requires to take a few narrow-band Raman images by fast switching the transmittance of the proposed programmable optical filter in front of the CCD, and the full spectrum at each pixel can be rapidly reconstructed by using spectral reconstruction algorithms. Since those spectral reconstruction algorithms are typically supervised learning method in nature, thus high computational efficiency can easily be achieved once the mathematic model has been trained. To evaluate the time efficiency, the spectral reconstruction algorithm used in this study is test on 90,000 cell's Raman spectra, corresponding to a spectral data cube with 300 pixels $\times$ 300 pixels $\times$ 907 wavenumbers. The spectral reconstruction algorithm was coded and tested in a computer with Intel Core i5-7200U 2.5GHz CPU, 8GB RAM, and Windows 10 operating system. The average computation time is around 0.28s, thus only slight contribution on the final time cost is expected because of its high computational efficiency. In addition, the DMD can reach a high binary pattern rate up to several thousand hertz and is consequently expected to achieve a fast switching rate of the transmittance. Thus, in a sample limited case [30], it is expected that the proposed spectral reconstruction based method when taking 6 narrow-band Raman images with programable optical filter is approximately 15,000 times, 50 times and 150 times faster than point-scanning, line-scanning and staring methods, respectively. What's more, only slight increment in acquisition time is necessary for the proposed spectral reconstruction based method, when higher spatial and spectral resolution is required. Thus, it is expected that the time efficiency improvement of the proposed spectral reconstruction method should be more significant if the required spatial and spectral resolution is much higher.

C. SPECTRAL DATA POST-PROCESSING BASED ON PROGRAMMABLE OPTICAL FILTER

For identifying occluded flaps and normal flaps from diffuse reflectance measurements, only single transmittance is necessary theoretically and the coding transmittance spectrum can be found in Fig. 9 (a). For synthesizing the coding transmittance spectrum of the programmable optical filter, the first 25 non-negative PCs are obtained from 102 sets of diffuse reflectance spectral data by non-negative PCA methods and then are compressed to one dimension by LDA model. However, since patterns involved negative component cannot be obtained by the proposed programmable optical filter, this single transmittance can be realized by dividing it into two sets of transmittance, i.e. compensation transmittance and imaging transmittance, in which the subtraction between those two sets of transmittance is identical to the original single coding transmittance, as shown in Fig. 9 (b). Two sets of narrow-band measurements are simulated by the inner product of diffuse reflectance measurements and those two transmittance spectra, respectively. The subtracted values of those two sets of narrow-band measurements are directly used for identifying occluded flaps and normal flaps,

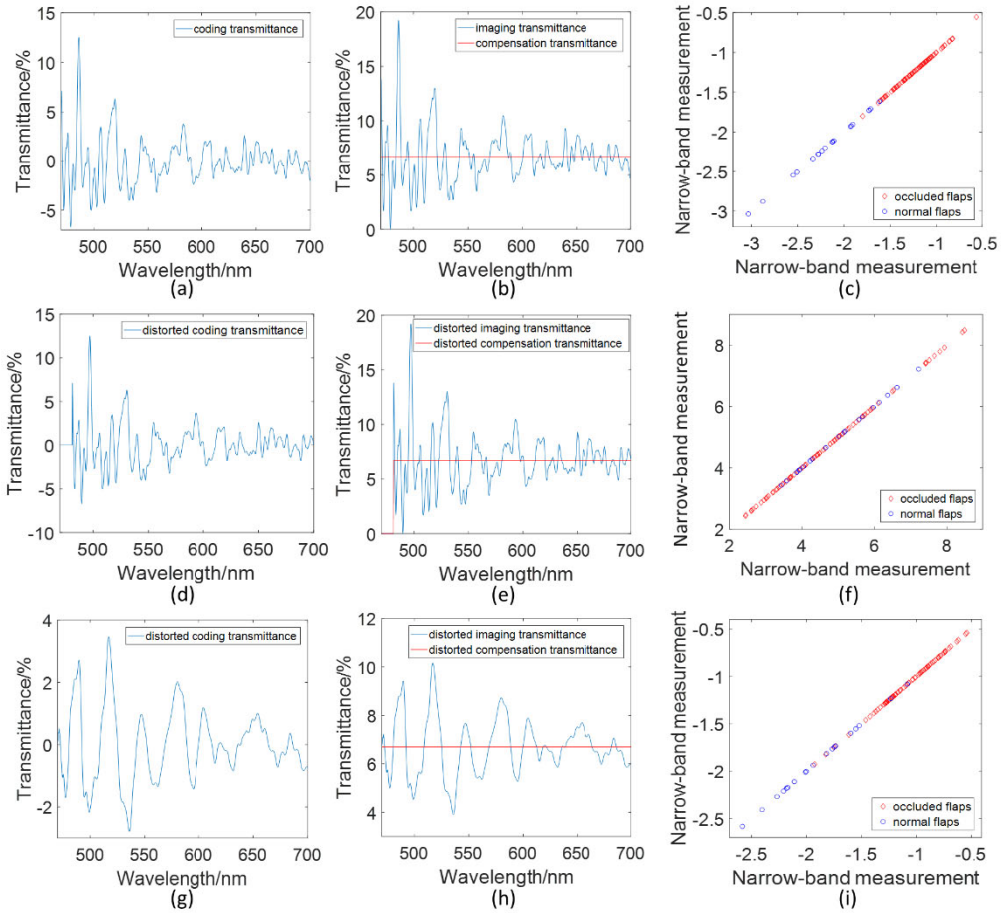

FIGURE 9. **Programmable optical filter based spectral data post-processing for diffuse reflectance measurements of occluded and normal flaps: (a)-(c) coding transmittance, imaging transmittance and compensation transmittance, and corresponding classification result based on narrow-band measurements; (d)-(f) distorted coding, imaging transmittance and compensation transmittance spectra by collimated beams with non-perpendicular incidence, and corresponding classification result based on narrow-band measurements; (g)-(i) distorted coding, imaging transmittance and compensation transmittance spectra by uncollimated beam, and corresponding classification result based on narrow-band measurements.**

as shown in Fig. 9 (c), and a classification accuracy of 98.04% is achieved, which is comparable to the result of conventional numerical methods in our previous study [22]. In addition, distorted transmittance spectra by both collimated beam with non-perpendicular incidence and uncollimated beam were used to investigate their impact on final classification accuracy. For distorted transmittance by uncollimated beam, the classification accuracy is 92.16%, which is close to that of conventional numerical method and reference transmittance by collimated beam with perpendicular incidence, as shown in Fig. 9 (g) to (i). However, the classification accuracy for distorted transmittance by collimated beams with non-perpendicular incidence is only 56.86%, which is much lower than the above results, as shown in Fig. 9 (d) to (f). The reason is that the distorted transmittance by uncollimated beam can still collect most of the important spectral information although the larger bandwidth leads to the collection of some useless spectral information, whereas the distorted transmittance by collimated beam with non-perpendicular incidence loses the most important spectral information due to the central wavelength shifts.

For identifying live, apoptosis and necrosis leukemia cells from Raman measurements, two transmittance spectra are necessary theoretically and the transmittance spectra can be found in Fig. 10 (a), in which the first ten PCs from 30 sets of Raman measurements are used and then are compressed into two dimensions. Similarly, in order to avoid negative transmittance, three transmittance spectra are used to mimic those two coding transmittance spectra. Three sets of narrow-band measurements are subsequently generated based on those three transmittance spectra and the subtracted values are directly used for identifying live, apoptosis and necrosis leukemia cells, as shown in Fig. 10 (b) and (c). A classification accuracy of 93.3% is achieved, which is exactly the same to the result of conventional numerical methods in our previous study [16]. Similarly, the classification accuracy for distorted transmittance by uncollimated beam is 90% and is comparable to that of conventional numerical method and

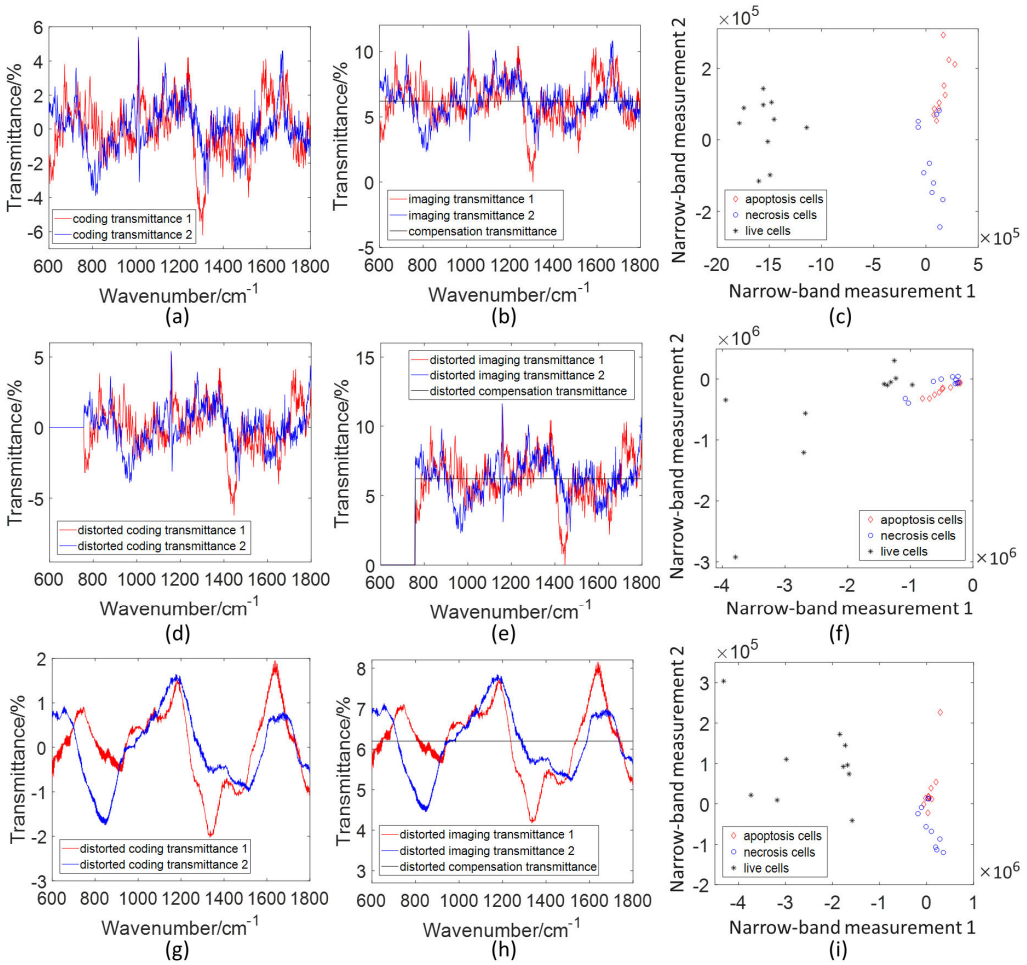

FIGURE 10. Programmable optical filter based spectral data post-processing for Raman measurements of live, apoptosis and necrosis leukemia cells: (a)-(c) coding transmittance, imaging transmittance and compensation transmittance, and corresponding classification result based on narrow-band measurements; (d)-(f) distorted coding, imaging transmittance and compensation transmittance spectra by collimated beams with non-perpendicular incidence, and corresponding classification result based on narrow-band measurements; (g)-(i) distorted coding, imaging transmittance and compensation transmittance spectra by uncollimated beam, and corresponding classification result based on narrow-band measurements.

reference transmittance by collimated beam with perpendicular incidence, whereas the classification accuracy for distorted transmittance by collimated beams with non-perpendicular incidence is only 70% and is much lower than the above results, as shown in Fig. 10 (d) to (i). Based on the above classification results of diffuse reflectance measurements and Raman measurements, it can be concluded that the classification accuracy of this programmable optical filter based spectral post-processing method is more susceptible to the collimation of incident beam other than perpendicularity. Thus, the calibration of the programmable optical filter is extremely necessary, especially for the perpendicularity of incident beam.

IV. CONCLUSSION

In this paper, a DMD-based 2D programmable optical filter was proposed and validated theoretically. Such programmable optical filter can achieve arbitrary transmittance, which is the key technique for fast spectroscopic imaging based on spectral reconstruction method and can significantly improve the spectral reconstruction accuracy when the spectral shape is complicated. Furthermore, its arbitrary transmittance enables hardware-based spectral data post-processing instead of the conventional numerical methods, thus the spectral data acquisition and analysis can be performed simultaneously and sped up significantly, especially when spectral imaging with large amounts of spectral data is necessary. Although ideal collimated beam with perpendicular incidence is difficult to be achieved in practical applications, only slight degradations on both spectral reconstruction accuracy and classification accuracy were found for uncollimated beam with perpendicular incidence and the perpendicularity of the incident beam should be not difficult to be calibrated. Therefore, the proposed 2D programmable optical filter should be feasible to be applied on fast spectroscopic imaging with high spatial and spectral resolution for

observing fast changing phenomena and even real-time target identification from micro to macro scale.

REFERENCES

[1] A. F. H. Goetz, G. Vane, J. E. Solomon, and B. N. Rock, "Imaging spectrometry for earth remote sensing," *Science*, vol. 228, no. 4704, pp. 1147–1153, 1985.

[2] F. Eugenio, J. Marcello, and J. Martin, "High-resolution maps of bathymetry and benthic habitats in shallow-water environments using multispectral remote sensing imagery," *IEEE Trans. Geosci. Remote Sens.*, vol. 53, no. 7, pp. 3539–3549, Jul. 2015.

[3] Z. Dionnet, A. Aleon-Toppani, D. Baklouti, F. Borondics, F. Brisset, Z. Djouadi, C. Sandt, and R. Brunetto, "Organic and mineralogic heterogeneity of the Paris meteorite followed by FTIR hyperspectral imaging," *Meteoritics Planetary Sci.*, vol. 53, no. 12, pp. 2608–2623, Dec. 2018.

[4] M. A. Hedegaard, M. S. Bergholt, and M. M. Stevens, "Quantitative multi-image analysis for biomedical Raman spectroscopic imaging," *J. Biophoton.*, vol. 9, no. 5, pp. 542–550, May 2016.

[5] A. Redo-Sanchez, B. Heshmat, A. Aghasi, S. Naqvi, M. Zhang, J. Romberg, and R. Raskar, "Terahertz time-gated spectral imaging for content extraction through layered structures," *Nat. Commun.*, vol. 7, pp. 1–7, Sep. 2016.

[6] Y. Garini, I. T. Young, and G. McNamara, "Spectral imaging: Principles and applications," *Cytol. A.*, vol. 69, no. 8, pp. 735–747, Aug. 2006.

[7] N. A. Hagen and M. W. Kudenov, "Review of snapshot spectral imaging technologies," *Opt. Eng.*, vol. 52, no. 9, pp. 090901-1–090901-23, Sep. 2013.

[8] S. Dhakal, K. Chao, J. Qin, M. Kim, Y. Peng, and D. Chan, "Identification and evaluation of composition in food powder using point-scan Raman spectral imaging," *Appl. Sci.*, vol. 7, p. 1, Dec. 2016.

[9] J. Qin, M. S. Kim, K. Chao, W. F. Schmidt, B. K. Cho, and S. R. Delwiche, "Line-scan Raman imaging and spectroscopy platform for surface and subsurface evaluation of food safety and quality," *J. Food Eng.*, vol. 198, pp. 17–27, Apr. 2017.

[10] Y. Inoue and J. Penuelas, "An AOTF-based hyperspectral imaging system for field use in ecophysiological and agricultural applications," *Int. J. Remote Sens.*, vol. 22, no. 18, pp. 3883–3888, Nov. 2010.

[11] Y. Peng and R. Lu, "An LCTF-based multispectral imaging system for estimation of apple fruit firmness: Part II. Selection of optimal wavelengths and development of prediction models," *Trans. ASABE*, vol. 49, no. 1, pp. 269–275, Nov. 2005.

[12] Q. Li, X. He, Y. Wang Y, Liu H, Xu D, Guo F, "Review of spectral imaging technology in biomedical engineering: Achievements and challenges," *J. Biomed. Opt.*, vol. 18, no. 10, Oct. 2013, Art. no. 100901.

[13] L. Gao and L. V. Wang, "A review of snapshot multidimensional optical imaging: Measuring photon tags in parallel," *Phys. Rep.*, vol. 616, pp. 1–37, Feb. 2016.

[14] G. R. Arce, D. J. Brady, L. Carin, H. Arguello, and D. S. Kittle, "Compressive coded aperture spectral imaging: An introduction," *IEEE Signal Process. Mag.*, vol. 31, no. 1, pp. 105–115, Jan. 2014.

[15] A. Wagadarikar, R. John, R. Willett, and D. Brady, "Single disperser design for coded aperture snapshot spectral imaging," *Appl. Opt.*, vol. 47, no. 10, pp. B44–B51, Apr. 2008.

[16] S. Chen, Y. H. Ong, and Q. Liu, "Fast reconstruction of Raman spectra from narrow-band measurements based on Wiener estimation," *J. Raman Spectrosc.*, vol. 44, no. 6, pp. 875–881, Jun. 2013.

[17] S. Chen, Y. H. Ong, X. Lin, and Q. Liu, "Optimization of advanced Wiener estimation methods for Raman reconstruction from narrow-band measurements in the presence of fluorescence background," *Biomed. Opt. Express*, vol. 6, no. 7, pp. 2633–2648, Jul. 2015.

[18] D. Wei, S. Chen, Y. H. Ong, C. Perlaki, and Q. Liu, "Fast wide-field Raman spectroscopic imaging based on simultaneous multi-channel image acquisition and Wiener estimation," *Opt. let.*, vol. 41, no. 12, pp. 2783–2786, Jun. 2016.

[19] S. Chen, X. Lin, C. Yuen, S. Padmanabhan, R. W. Beuerman, and Q. Liu, "Recovery of Raman spectra with low signal-to-noise ratio using Wiener estimation," *Opt. Express*, vol. 22, no. 10, pp. 12102–12114, May 2014.

[20] D. S. Wilcox, G. T. Buzzard, B. J. Lucier, P. Wang, and D. Ben-Amotz, "Photon level chemical classification using digital compressive detection," *Anal. Chim. Acta.*, vol. 755, pp. 17–27, Nov. 2012.

[21] O. G. Rehrauer, V. C. Dinh, B. R. Mankani, G. T. Buzzard, B. J. Lucier, and D. Ben-Amotz, "Binary complementary filters for compressive Raman spectroscopy," *Appl. Spectrosc.*, vol. 72, no. 1, pp. 69–78, Jul. 2018.

[22] S. Chen, G. Wang, X. Cui, and Q. Liu, "Stepwise method based on Wiener estimation for spectral reconstruction in spectroscopic Raman imaging," *Opt. Express*, vol. 25, no. 2, pp. 1005–1018, Jan. 2017.

[23] R. Piché, "Nonnegative color spectrum analysis filters from principal component analysis characteristic spectra," *J. Opt. Soc. Amer. A*, vol. 19, no. 10, pp. 1946–1950, Oct. 2002.

[24] S. Chen, L. Kong, W. Xu, X. Cui, and Q. Liu, "A fast fluorescence background suppression method for Raman spectroscopy based on stepwise spectral reconstruction," *IEEE Access*, vol. 6, pp. 67709–67717, 2018.

[25] S. Chen, C. Zhu, C. C. Hoe-Kong, G. Sheoran, B. K. Tan, and Q. Liu, "Spectral diffuse reflectance and autofluorescence imaging can perform early prediction of blood vessel occlusion in skin flaps," *J. Biophoton.*, vol. 10, no. 12, pp. 1665–1675, Dec. 2017.

[26] V. Mazet, C. Carteret, D. Brie, J. Idier, and B. Humbert, "Background removal from spectra by designing and minimising a non-quadratic cost function," *Chemometr. Intell. Lab.*, vol. 76, no. 2, pp. 121–133, Feb. 2005.

[27] S. Chen, S. Zhu, X. Cui, W. Xu, C. Kong, Z. Zhang, and W. Qian, "Identifying non-muscle-invasive and muscle-invasive bladder cancer based on blood serum surface-enhanced Raman spectroscopy," *Biomed. Opt. Express*, vol. 10, no. 7, pp. 3533–3544, Jul. 2019.

[28] C. Zhu, S. Chen, C. H. Chui, B. K. Tan, and Q. Liu, "Early detection and differentiation of venous and arterial occlusion in skin flaps using visible diffuse reflectance spectroscopy and autofluorescence spectroscopy," *Biomed. Opt. Express*, vol. 7, no. 2, pp. 570–580, Jan. 2016.

[29] Y. H. Ong, M. Lim, and Q. Liu, "Comparison of principal component analysis and biochemical component analysis in Raman spectroscopy for the discrimination of apoptosis and necrosis in K562 leukemia cells," *Opt. Express*, vol. 20, no. 20, pp. 22158–22171, Oct. 2012.

[30] S. Schlücker, M. D. Schaeberle, S. W. Huffman, and I. W. Levin, "Raman microspectroscopy: A comparison of point, line, and wide-field imaging methodologies," *Anal. Chem.*, vol. 75, no. 16, pp. 4312–4318, Jul. 2003.

JIAO LU received the bachelor's degree from the Liao Ning Institute of Science Technology, China, and the master's degree from Northeastern University, China, where she is currently pursuing the Ph.D. degree with the College of Medicine and Biological Information Engineering. Her research interest includes fast spectroscopic imaging in biomedical applications.

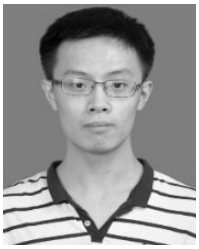

YUETIAN REN received the bachelor's degree from Northeastern University, China, where he is currently pursuing the master's degree with the College of Medicine and Biological Information Engineering. His research interest includes multispectral fundus imaging.

WENBIN XU received the Ph.D. degree in optical engineering from the University of Chinese Academy of Sciences. He is currently a Senior Engineer with the Science and Technology on Optical Radiation Laboratory, Beijing Institute of Environmental Features. His research interests include infrared spectroscopy and spectral data processing in industrial applications.

XIAOYU CUI received the bachelor's degree from the Shenyang University of Technology, China, and the master's and Ph.D. degrees in biomedical engineering from Northeastern University, China, where he is currently an Associate Professor with the College of Medicine and Biological Information Engineering. His research interests include optical imaging and machine learning in biomedical applications.

LIPING XIE received the bachelor's and master's degrees from Jilin University, China, in 2008 and 2010, respectively, and the Ph.D. degree from Tsinghua University, China, in 2014. She is currently with Northeastern University. Her research interests include stretchable electronic materials and devices, and biosensing.

SHUO CHEN received the bachelor's degree from Shanghai Jiao Tong University, China, the master's degree from Heidelberg University, Germany, and the Ph.D. degree from the School of Chemical and Biomedical Engineering, Nanyang Technological University, Singapore. He is currently an Associate Professor with the College of Medicine and Biological Information Engineering, Northeastern University, China. His research interest includes fast spectroscopic imaging in biomedical applications.

JINHONG GUO received the bachelor's degree in electronic engineering from the University of Electronic Science and Technology of China, Chengdu, China, in 2010, and the Ph.D. degree in biomedical engineering from Nanyang Technological University, Singapore, in 2014.

From 2014 to 2015, he was a Postdoctoral Fellow working on the pillar of engineering design with MIT-SUTD, Singapore. From January 2016 to July 2016, he was a Visiting Professor with the School of Mechanical Engineering, University of Michigan, Ann Arbor. He is currently a Full Professor with the School of Communication and Information Engineering, University of Electronic Science and Technology of China, and also with the Chengdu University of Chinese Traditional Medicine, Chengdu. He has authored or coauthored more than 70 publications in top journal, such as IEEE TII, TBME, TBioCAS, *Analytical Chemistry*, and *Biosensor and Bioelectronics*. His current research interests include electrochemical sensor and lab-on-a-chip devices for point of care test toward clinical use.

Dr. Guo was a recipient of the China Sichuan Thousand Talents Plan for Scholars Award, in 2015 and the Chengdu Expert in Science and Technology Award, in 2015. He is also appointed as the Chief Scientist with Longmaster Information Company Ltd. (one listed corporation in China, stock ID: 300288), who is in charge of the Research and Development Center for POCT.

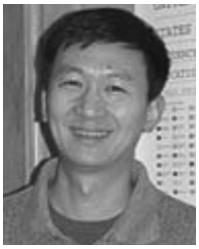

YUDONG YAO received the B.Eng. and M.Eng. degrees from the Nanjing University of Posts and Telecommunications, Nanjing, China, in 1982 and 1985, respectively, and the Ph.D. degree from Southeast University, Nanjing, in 1988, all in electrical engineering. From 1989 and 1990, he was with Carleton University, Ottawa, Canada, as a Research Associate working on mobile radio communications. From 1990 to 1994, he was with Spar Aerospace Ltd., Montreal, Canada, where he was involved in research on satellite communications. From 1994 to 2000, he was with Qualcomm, Inc., San Diego, CA, USA, where he participated in research and development in wireless code-division multipleaccess (CDMA) systems. Since 2000, he has been with the Stevens Institute of Technology, Hoboken, NJ, USA, where he is currently a Professor and the Department Director of electrical and computer engineering. He is also an Adjunct Professor with the College of Medicine and Biological Information Engineering, Northeastern University, China. He is the holder one Chinese patent and 12 U.S. patents. His research interests include wireless communications and networks, spread spectrum and CDMA, antenna arrays and beamforming, cognitive and software-defined radio, and digital signal processing for wireless systems.